

Cite this: *Chem. Sci.*, 2021, 12, 2527

All publication charges for this article have been paid for by the Royal Society of Chemistry

# Mechanistic insights into rhodium-catalyzed enantioselective allylic alkylation for quaternary stereogenic centers†

Monika Pareek and Raghavan B. Sunoj \*

Installing quaternary stereogenic carbon is an arduous task of contemporary importance in the domain of asymmetric catalysis. To this end, an asymmetric allylic alkylation of  $\alpha,\alpha$ -disubstituted aldehydes by using allyl benzoate in the presence of Wilkinson's catalyst [Rh(Cl)(PPh<sub>3</sub>)<sub>3</sub>], (*R*)-BINOL-P(OMe) as the external ligand, and LiHMDS as the base has been reported to offer high enantioselectivity. The mechanistic details of this important reaction remain vague, which prompted us to undertake a detailed density functional theory (SMD<sub>(THF)</sub>/B3LYP-D3) investigation on the nature of the potential active catalyst, energetic features of the catalytic cycle, and the origin of high enantioselectivity. We note that a chloride displacement from the native Rh-phosphine [Rh(Cl)(PPh<sub>3</sub>)<sub>3</sub>] by BINOL-P(OMe) phosphite and an ensuing MeCl elimination can result in the *in situ* formation of a Rh-phosphonate [Rh(BINOL-P=O)(PPh<sub>3</sub>)<sub>3</sub>]. A superior energetic span ( $\delta E$ ) noted with such a Rh-phosphonate suggests that it is likely to serve as an active catalyst. The uptake of allyl benzoate by the active catalyst followed by the turnover determining C–O bond oxidative addition furnishes a Rh- $\pi$ -allyl intermediate, which upon interception by (*Z*)-Li-enolate (derived from  $\alpha,\alpha$ -disubstituted aldehyde) in the enantiocontrolling C–C bond generates a quaternary stereogenic center. The addition of the *re* prochiral face of the (*Z*)-Li-enolate to the Rh-bound allyl moiety leading to the *R* enantiomer of the product is found to be 2.4 kcal mol<sup>-1</sup> more preferred over the addition through its *si* face. The origin of the stereochemical preference for the *re* face addition is traced to improved noncovalent interactions (NCIs) and less distortion in the enantiocontrolling C–C bond formation transition state than that in the *si* face addition. Computed enantioselectivity (96%) is in very good agreement with the experimental value (92%), so is the overall activation barrier ( $\delta E$  of 17.1 kcal mol<sup>-1</sup>), which is in conformity with room temperature reaction conditions.

Received 8th September 2020  
Accepted 15th December 2020

DOI: 10.1039/d0sc04959j

rsc.li/chemical-science

## Introduction

The significant progress in the field of asymmetric catalysis in the last few decades helped in realizing complex organic target molecules of practical significance. The presence of quaternary carbon stereogenic centers in natural products, drugs, and biologically active molecules has been an inspiration toward developing asymmetric synthesis for such structural motifs.<sup>1</sup> For a long time, molecules containing quaternary carbon stereogenic centers have mostly been derived from natural product precursors such as terpenoids rather than building them through chemical synthesis.<sup>2</sup> Traditional chemical synthesis relying on Diels–Alder reactions, asymmetric allylic alkylation of chiral carbon nucleophiles, and intramolecular Heck reactions has also found interesting use.<sup>3</sup> Over the years, there have been a remarkable number of efforts in installing quaternary

carbon stereogenic centers on cyclic systems by using a myriad of protocols such as biocatalysis, organocatalysis, and transition metal catalysis.<sup>4</sup> The enantioselective synthesis of quaternary carbon stereogenic centers in acyclic systems has been regarded as far more challenging.<sup>5</sup> Recent trends in this front indicate the use of transition metal catalysis for effectively engaging achiral as well as racemic substrates as the starting material.

The Tsuji–Trost reaction continues to be the most common choice for the generation of acyclic quaternary carbon stereogenic centers.<sup>6</sup> Direct asymmetric allylic alkylation of enolates derived from aldehydes can also provide direct access to quaternary stereogenic centers. In particular, the List group reported an enantioselective  $\alpha$ -allylation of  $\alpha$ -branched aldehydes by employing a chiral phosphate anion as a source for chiral induction.<sup>7</sup> In a related Tsuji–Trost allylation by the Yoshida group, a chiral  $\alpha$ -amino acid derived enamine of  $\alpha$ -branched aldehydes is used in conjunction with allyl esters activated by an achiral Pd catalyst toward realizing quaternary stereogenic carbon centers in high enantioselectivity.<sup>8</sup> Most recently, the Stoltz as well as the Marek groups have reported an

Department of Chemistry, Indian Institute of Technology Bombay, Powai, Mumbai 400076, India. E-mail: sunoj@chem.iitb.ac.in

† Electronic supplementary information (ESI) available. See DOI: 10.1039/d0sc04959j



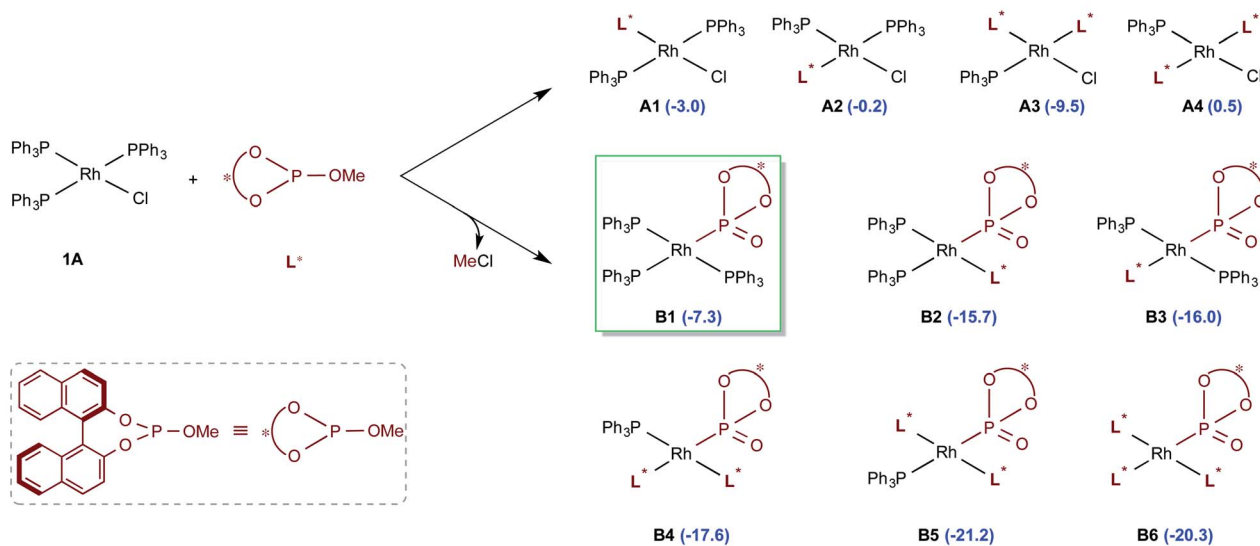


competing diastereomeric transition states.<sup>25</sup> The efficiency of the catalytic cycle was computed by using the Shaik-Kozuch energetic span model.<sup>26</sup>

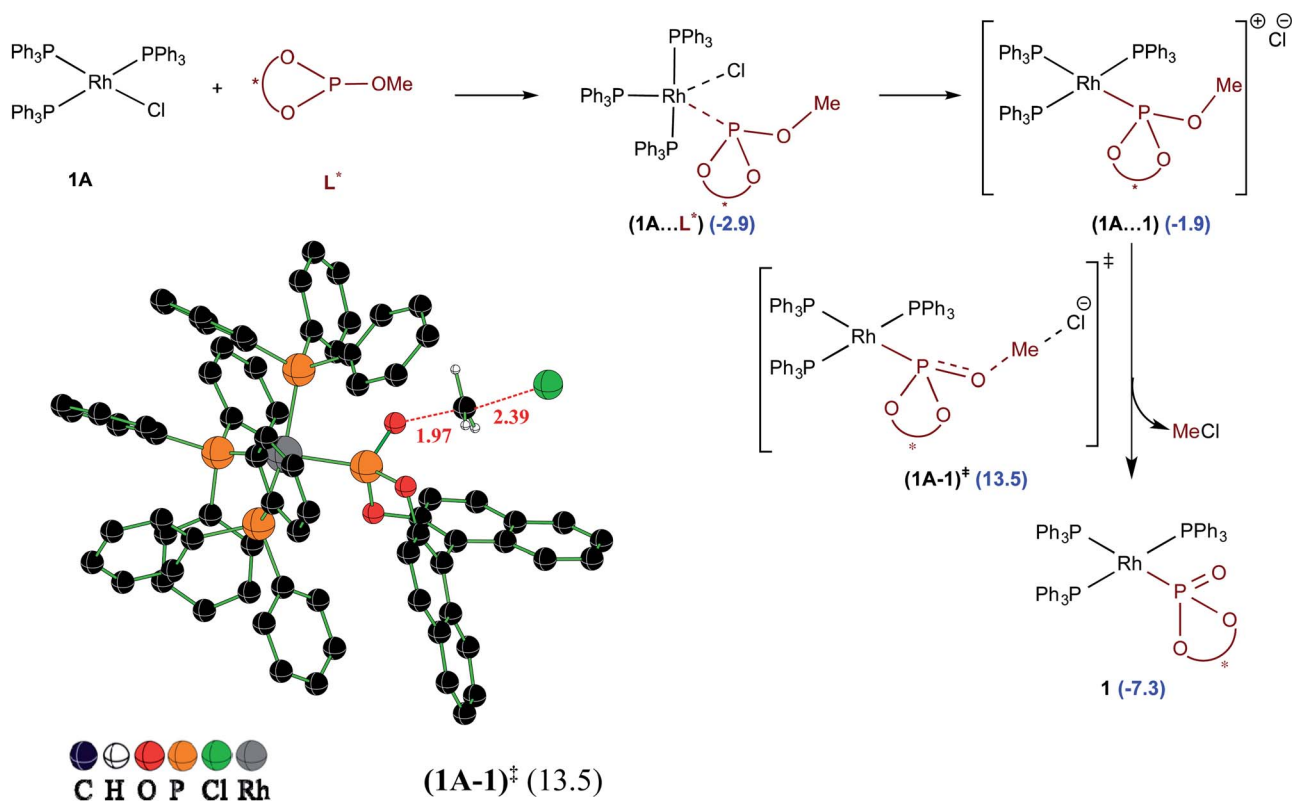
## Results and discussion

A careful examination of the reported experimental protocol is pertinent to various mechanistic scenarios considered in this

### (a) The formation of different likely active catalysts differing in their ligand combinations



### (b) Mechanism of Rh-catalyzed Arbuzov rearrangement



Scheme 2 (a) The relative Gibbs free energies of the formation (in kcal mol<sup>-1</sup>) of different likely active species computed with respect to the separated reactants. (b) Important steps in the conversion of Rh-bound BINOL-methyl phosphite to the corresponding phosphonate ligand through the Rh-Arbuzov rearrangement and a representative example of an optimized geometry for the expulsion of methyl chloride. Any of the active catalysts listed here is assigned a general notion **1** when it is considered in the catalytic cycle as shown in Scheme 3.



study. The procedure involves combining Wilkinson's catalyst (**1A**) with the chiral ligand (*R*)-BINOL-*P*(OMe) (**L\***) in tetrahydrofuran (THF) solvent, which could lead to the formation of a number of analogs of Wilkinson's catalyst. The additive *N,N'*-dimethylpropyleneurea (DMPU) and the substrates (2-phenylbutanal (**5**) and allyl benzoate (**2**)) were sequentially introduced, which was followed by drop-wise addition of lithium bis(trimethylsilyl)amide (LiHMDS) in THF.<sup>27</sup> Given this, we have examined the energetic feasibilities of the formation of different variants of Wilkinson's catalyst by exchanging the labile Rh-bound triphenylphosphines (PPh<sub>3</sub>) with other ligands such as the chiral BINOL-phosphite. We note that the use of modified Wilkinson's catalyst has gained recent popularity, including that in asymmetric allylic alkylation reactions.<sup>14c,d</sup>

Shown in Scheme 2 are different species that could possibly be generated through ligand exchange with Wilkinson's catalyst and the corresponding relative Gibbs free energies of their formation with respect to **1A** and **L\***. Some of these species could serve as a potential active catalyst in this reaction. The species denoted as **A1–A4** can be formed by exchanging the native phosphine(s) with the chiral BINOL phosphite (**L\***)

ligand(s), where the latter is used four times more than **1A**. The substitution of two of the phosphine ligands by **L\***, leading to **A3**, is found to be the most favorable possibility in this series (Scheme 2(a)).<sup>28</sup> Another interesting alternative arises when the chiral BINOL-phosphite displaces the native chloride instead of the phosphine ligands, leading to an ion-pair intermediate (**1A⋯1**) as shown in Scheme 2(b). An S<sub>N</sub>2 type rebound of the displaced chloride on the -OMe moiety can then facilitate a Rh-catalyzed Arbuzov rearrangement (analogous to Michaelis-Arbuzov rearrangement involving alkyl halides), wherein the release of MeCl can result in the *in situ* formation of a phosphonate **B1**.<sup>29</sup> We note that the barrier for the MeCl expulsion, computed with respect to the preceding ion-pair intermediate, is 16.4 kcal mol<sup>-1</sup>, which is affordable under room temperature conditions.<sup>30</sup> Since an excess of BINOL-phosphite (**L\***) was used in the experiments, the initially formed **B1** could also undergo further ligand exchanges to form species such as **B2–B6**.

The relative Gibbs free energies provided in Scheme 2 suggest that the formation of most of the mixed ligand combinations of the Rh-phosphonates is thermodynamically feasible, hinting at their simultaneous existence and potential



Scheme 3 The key mechanistic steps involved in the Rh-catalyzed asymmetric allylic alkylation of 2-phenylbutanal by allyl benzoate.



participation in the reaction. For ease of discussion on the broad mechanistic features shown in Scheme 3, we shall consider that the active catalyst entering the catalytic cycle is denoted as **1**, which could potentially be any variant of Wilkinson's catalyst. The active species **1** can bind to one of the substrates, namely, allyl benzoate (**2**), through an  $\eta^2$  coordination to form a catalyst–substrate complex **3**. Intermediate **3** can then undergo C–O bond oxidative addition *via* a transition state (**3–4**)<sup>‡</sup> to form an  $\eta^3$ -Rh- $\pi$ -allyl intermediate **4**.<sup>31</sup> In a concurrent event, the action of LiHMDS on the pro-nucleophilic 2-phenylbutanal (**5**) helps in generating the desired lithium enolate (**6**). The next step is enantioselective C–C bond formation through a transition state (**4–7**)<sup>‡</sup>, wherein the nucleophilic lithium enolate **6** adds to the electrophilic Rh- $\pi$ -allyl intermediate **4** to form an  $\eta^2$  catalyst–product complex (**7**). In the last step, ligand exchange with PPh<sub>3</sub> can help release the final product (**8**) besides regenerating the active species **1** so as to continue the catalytic cycle with the fresh uptake of a new substrate molecule.

The overall catalytic cycle, as shown in Scheme 3, is examined in greater detail to identify the energetically most preferred pathway. Since the formation of several likely active species is found to be exoergic (Scheme 2), we have considered different ligand combinations around the Rh in the vital C–O bond oxidative addition transition state (**3–4**)<sup>‡</sup>. The elementary step barriers for the oxidative addition compiled in Table 1 suggest that active species such as **A1** and **A3** bearing the native ligands on the Rh center are quite unlikely to serve as the actual catalytic entity under the given reaction conditions. An active engagement of the base, in the form of LiHMDS·3DMPU, is therefore examined to see whether it is likely to lower the transition state energies through explicit coordination to the allyl benzoate oxygen. It is instructive to draw certain parallels between our mechanistic model and the experimental

procedure such as the use of an equimolar amount (0.95 mmol) of the base and the additive (DMPU). In the THF solvent, LiHMDS is known to exist in equilibrium between its dimer and monomer, with 3 coordinated THF on the Li.<sup>32</sup> Although the role of DMPU is typically to prevent the aggregation of Li-enolates,<sup>33</sup> the improved yield observed upon the inclusion of DMPU alludes to a more active molecular role. In view of this, explicit coordination of DMPU by displacing the Li-bound THF molecules is considered to find that the formation of species such as LiHMDS·3DMPU is energetically feasible.<sup>32f</sup> The role of the base and its mode of participation in the C–O bond oxidative addition transition state can now be better understood. The relative Gibbs free energies of these transition states, given in Table 1, suggest that a direct participation of both the base and the additive in the OA transition state is energetically more beneficial as compared to the corresponding base-free mode.<sup>34</sup>

In our attempts to find various possibilities for the Li-bound OA TS (**3–4**)<sup>‡</sup> it is identified that the displacement of two DMPU molecules from LiHMDS·3DMPU by the oxygen atoms of the benzoate and BINOL phosphonate is quite likely. In Table 1, such binding modes are listed as LiHMDS·1DMPU against each of the likely active species (**A1** through **B4**). The exoergic formation of different likely active catalysts (Scheme 2) prompted us to consider their participation in the catalytic cycle. Since the C–O bond oxidative addition is the first key step wherein the active catalyst comes in contact with the substrate such as the allyl benzoate (**2**), we have evaluated the role of all these active catalysts in the C–O bond oxidative addition transition state (**3–4**)<sup>‡</sup>. These possibilities differ in terms of the number of Rh-bound phosphine/phosphonate ligands and their relative geometric dispositions in (**3–4**)<sup>‡</sup>. In order to afford a direct comparison between the OA TSs involving different active catalysts, the activation barrier is calculated with respect to the respective active catalyst (Table 1). The active catalyst (denoted as **1** in Scheme 3) that provides the lowest elementary step barrier for (**3–4**)<sup>‡</sup> is considered for the next stereoselective C–C bond formation step in this study. We note that the lower energy ligand combinations in the potential active catalysts belonging to the **A** series exhibit higher elementary step barriers (23.7 and 29.7 kcal mol<sup>−1</sup> respectively for **A1** and **A3**) for the oxidative addition transition state (**3–4**)<sup>‡</sup>.<sup>35</sup> Similarly, in the case of potential active catalysts in the **B** series, the lowest elementary step barrier for oxidative addition is found to be 17.1 kcal mol<sup>−1</sup> with **B1**, which is therefore considered as the most likely active catalyst that follows the minimum energy path.<sup>36</sup> The optimized geometry of the most likely OA transition state (**3–4**)<sup>‡</sup> with **B1** is shown in Fig. 1. The C–O bond oxidative addition transition state leads to the formation of an  $\eta^3$ -Rh- $\pi$ -allyl intermediate (**4**).

Once the electrophilic partner **4** ( $\eta^3$ -Rh- $\pi$ -allyl intermediate) is available, it can be intercepted by the Li-enolate (**6**). It is important to pay careful attention to the energetics of the formation of *E* and *Z* configurations of **6** as the stereochemical outcome of the reaction could have a critical dependence on the enolate configuration involved in the ensuing C–C bond formation with the Rh- $\pi$ -allyl intermediate (*vide infra*). In an acyclic  $\alpha$ -branched aldehyde, the free rotation along the C $\alpha$ –

**Table 1** The relative Gibbs free energies ( $\Delta G_{\text{rel}}$  in kcal mol<sup>−1</sup>) for the C–O bond oxidative addition transition state (**3–4**)<sup>‡</sup> with respect to the separated reactants and the elementary step barriers ( $\Delta G_{\text{barrier}}$ ) with respect to the corresponding preceding intermediates<sup>a</sup>

(3–4) <sup>‡</sup>	Absence of the base		LiHMDS·1DMPU	
	$\Delta G_{\text{rel}}$	$\Delta G_{\text{barrier}}$	$\Delta G_{\text{rel}}$	$\Delta G_{\text{barrier}}$
<b>A1</b>	24.5	27.5	20.7	23.7
<b>A3</b>	26.9	36.4	20.2	29.7
<b>B1</b>	<b>21.6</b>	<b>28.9</b>	<b>9.8</b>	<b>17.1</b>
<b>B2</b>	<sup>a</sup>	<sup>b</sup>	5.4	21.1
<b>B3</b>	20.8	36.8	2.0	18.0
<b>B4</b>	16.2	33.8	2.0	19.6

<sup>a</sup> The lowest energy ligand combinations of the potential active catalyst series **A** (**A1** and **A3** as shown in Scheme 2) have been considered in the C–O bond oxidative addition transition state. In the case of series **B**, the incoming substrate is likely to displace the PPh<sub>3</sub> ligand to form the catalyst–substrate complex, which would therefore be similar for both **B4** and **B5**. Similarly, the substrate uptake by **B6** by displacing one of the BINOL-phosphite ligands (L\*) would make it similar to the substrate–catalyst complex derived from **B4**/**B5**. Hence, only **B4** is presented here. <sup>b</sup> The transition state failed to converge even after repeated attempts.





Fig. 1 Optimized geometry of the transition state  $(3-4)^\ddagger$  for the C–O bond oxidative addition, leading to the formation of a Rh- $\pi$ -allyl intermediate. Relative Gibbs free energy (in kcal mol<sup>-1</sup>) given in parentheses is with respect to the separated reactants with **B1** as the active catalyst. Distances are in Å.

C(carbonyl) bond, shown as C2–C3 in Fig. 2, presents two important modes for deprotonation, one leading to **6<sub>E</sub>** and the other to **6<sub>Z</sub>** enolate.<sup>37</sup> The relative Gibbs free energy barriers for the LiHMDS promoted deprotonation indicate that the *Z* enolate is kinetically more favored by 1.3 kcal mol<sup>-1</sup> than the *E* enolate.<sup>38</sup> Interesting differences in the pattern of the intramolecular noncovalent interactions between  $(5-6)_Z^\ddagger$  and  $(5-6)_E^\ddagger$

are noted as a key contributor to *Z*-selectivity.<sup>39</sup> The C–H $\cdots$ O (a') interaction between the phenyl and the carbonyl oxygen noted in  $(5-6)_Z^\ddagger$  leading to the *Z* enolate is absent in the *E* enolate. The C–H $\cdots$ O noncovalent interactions (b' and c') are also noted between the methyl group on the DMPU and the carbonyl oxygen in both the *Z* and *E* enolates. The C–H $\cdots$  $\pi$  interaction is also found between the methyl group on the LiHMDS and the

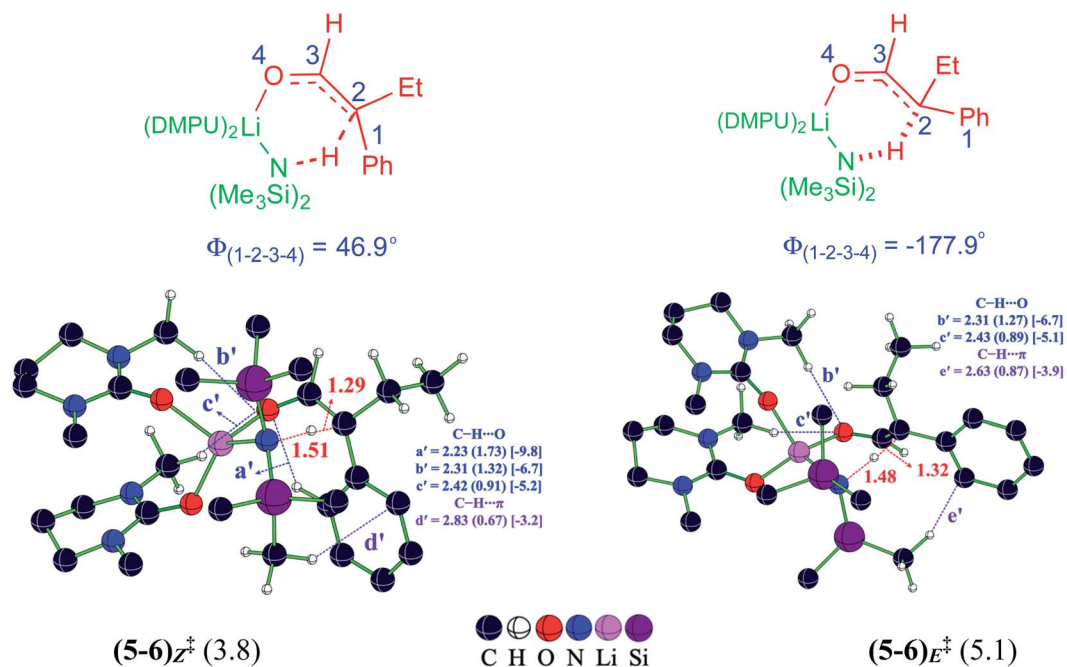


Fig. 2 Optimized transition state geometries for the LiHMDS promoted deprotonation leading to Li-enolates. Important interatomic distances (in Å) and the corresponding electron densities ( $\rho \times 10^{-2}$ ) at the bond critical points are shown in parentheses along with the strength of the respective noncovalent interactions (in kcal mol<sup>-1</sup>) in square brackets. The relative Gibbs free energy barriers for deprotonation computed with respect to the separated reactants are in kcal mol<sup>-1</sup>.



phenyl of the  $\alpha,\alpha$ -disubstituted aldehyde in both the  $Z$  ( $d'$ ) and  $E$  ( $e'$ ) enolates.

Until now, the formation of the electrophilic partner in the form of a Rh- $\pi$ -allyl intermediate (**4**) and Li-enolate (**6**) as the nucleophilic counterpart is presented. When both of these key reactants become available, the next vital event, *i.e.*, the C-C bond formation, can take place. To locate the most preferred C-C bond formation transition state, generally denoted as (**4-7**)<sup>‡</sup> in this manuscript, we have considered the addition of the Li-enolate **6<sub>Z</sub>** through its *si* and *re* prochiral faces and examined various conformational possibilities that differ in the dihedral angle along the incipient C-C bond.<sup>40</sup> Certain general features of these stereoinducing TSS are (a) the anchoring role of the tetracoordinate Li in holding both the enolate and Rh- $\pi$ -allyl moieties together, latter through the benzoate oxygen, and (b) the changes in the noncovalent interactions (NCIs) depending on the prochiral face of the enolate involved in the bond formation. More importantly, the enolate addition through its *re* face is found to be energetically more preferred over the *si* face addition. The relative Gibbs free energy difference of 2.4 kcal mol<sup>-1</sup> between these diastereomeric transition states

corresponds to a 96% enantiomeric excess.<sup>41</sup> The optimized geometry for the lowest energy transition state (**4-7**)<sub>*re*</sub><sup>‡</sup> and its diastereomeric counterpart, along with the mapping of the NCIs, are shown in Fig. 3.

We sought additional details on the factors that contribute to the energy difference between the C-C bond formation transition states (**4-7**)<sub>*re*</sub><sup>‡</sup> and (**4-7**)<sub>*si*</sub><sup>‡</sup> by analyzing the NCIs as deciphered using the AIM analysis.<sup>42</sup> An approximate measure of NCI is deduced from the electron density at the bond critical point ( $\rho_{\text{bcp}}$ ) along various bond paths noticed in the topological analysis of the electron density.<sup>43</sup> In addition, the quantification of the NCIs is performed by using Espinosa's formulation that employs the topological parameters of the electron density distribution as obtained from the atoms in molecule formalism.<sup>44</sup> The strength of the individual interactions that contribute to the cumulative effect could therefore be estimated. It can be noted that the transition states (**4-7**)<sub>*re*</sub><sup>‡</sup> and (**4-7**)<sub>*si*</sub><sup>‡</sup> shown in Fig. 3 are well decorated with NCIs such as C-H $\cdots$  $\pi$ , C-H $\cdots$ O,  $\pi\cdots\pi$ , C-H $\cdots$ N and lone pair(O) $\cdots\pi$ . A comparison of the geometries of (**4-7**)<sub>*re*</sub><sup>‡</sup> and (**4-7**)<sub>*si*</sub><sup>‡</sup> reveals important differences in the NCIs depending on the prochiral face of the



Fig. 3 Optimized transition state geometries for the enantioselective C-C bond formation between the Li-enolate (**6<sub>Z</sub>**) and Rh- $\pi$ -allyl intermediate (**4**). Important interatomic distances (in Å) and the corresponding electron densities ( $\rho \times 10^{-2}$ ) at the bond critical points are shown in parentheses along with the strength of the respective noncovalent interactions (in kcal mol<sup>-1</sup>) in square brackets. The relative Gibbs free energies with respect to the lowest energy transition state are in kcal mol<sup>-1</sup>.



Li-enolate that participates in the C–C bond formation. In the lower energy diastereomeric transition state  $(4-7)_{re}^\ddagger$ , a C–H $\cdots$ O contact (denoted as a) is noted between the phenyl ring of the benzoate and the BINOL phosphonate oxygen. Additional two C–H $\cdots$ O contacts are also identified in  $(4-7)_{re}^\ddagger$ , which are between the equatorial PPh<sub>3</sub> ligand and the benzoate oxygen (h) as well as one between the phenyl ring of the benzoate and the BINOL phosphonate oxygen (j). The key differences in the NCIs found in the higher energy transition state  $(4-7)_{si}^\ddagger$  are as follows: the C–H $\cdots$ O contacts between DMPU and (i) phosphonate oxygen (b and c) and (ii) the benzoate oxygen (o) and one between the Rh- $\pi$ -allyl moiety and the enolate oxygen (m). Besides the C–H $\cdots$ O interactions, there are more number of C–H $\cdots$  $\pi$  contacts in the lower energy transition state  $(4-7)_{re}^\ddagger$  as compared to that in  $(4-7)_{si}^\ddagger$ . The three C–H $\cdots$  $\pi$  contacts (d, f, and g) are noted in  $(4-7)_{re}^\ddagger$ , whereas only one such interaction (e) is found in  $(4-7)_{si}^\ddagger$  between the axial PPh<sub>3</sub> ligand and the Rh- $\pi$ -allyl moiety. One C–H $\cdots$  $\pi$  contact (l) is also found between the methyl of DMPU and the phenyl ring of the benzoate group. This interaction is present in both  $(4-7)_{re}^\ddagger$  and  $(4-7)_{si}^\ddagger$ . The two different NCIs, a lone pair(O) $\cdots$  $\pi$  (i) (involving the benzoate oxygen and the equatorial PPh<sub>3</sub> ligand) and a  $\pi\cdots\pi$  (n) interaction (between the Rh- $\pi$ -allyl and the phenyl of the Li-enolate), are found in the higher energy transition state  $(4-7)_{si}^\ddagger$ , whereas a C–H $\cdots$ N (k) interaction is noted in the lower energy transition state  $(4-7)_{re}^\ddagger$  (between Rh- $\pi$ -allyl and the DMPU nitrogen). The

estimated strength of NCIs in the lower energy transition state  $(4-7)_{re}^\ddagger$  is found to be  $-46.9$  kcal mol<sup>-1</sup>, while that in the higher energy transition state  $(4-7)_{si}^\ddagger$  is  $-44.8$  kcal mol<sup>-1</sup>, indicating an additional 2.1 kcal mol<sup>-1</sup> stabilization in the former. The noncovalent interaction plots (NCI plots) are also generated to analyze the broader regions of NCIs between the interacting atoms/groups in these enantiocontrolling transition states.<sup>45</sup>

In addition to the NCI based analysis presented above, the origin of the energy difference between  $(4-7)_{re}^\ddagger$  and  $(4-7)_{si}^\ddagger$  is probed in greater detail by using activation strain analysis. The activation energy ( $\Delta E^\ddagger$ ) is considered as the sum of destabilizing distortion ( $\Delta E_d^\ddagger$ ) and stabilizing interaction ( $\Delta E_f^\ddagger$ ) energies in the transition state, calculated with respect to the lower energy transition state  $(4-7)_{re}^\ddagger$ . The distortion  $\Delta E_d^\ddagger$  is found to be 4.9 kcal mol<sup>-1</sup> higher in the higher energy transition state  $(4-7)_{si}^\ddagger$  than the corresponding value in  $(4-7)_{re}^\ddagger$ . However, the stabilizing  $\Delta E_f^\ddagger$  in the higher energy transition state  $(4-7)_{si}^\ddagger$  is found to be 2.2 kcal mol<sup>-1</sup> more than that in the lower energy diastereomeric counterpart  $(4-7)_{re}^\ddagger$ .<sup>46</sup> It is noted that in the higher energy transition state  $(4-7)_{si}^\ddagger$ , the Rh- $\pi$ -allyl fragment experiences 4.2 kcal mol<sup>-1</sup> more distortion as compared to that found in  $(4-7)_{re}^\ddagger$ . The net effect of  $\Delta E_d^\ddagger$  and  $\Delta E_f^\ddagger$  provides the transition state  $(4-7)_{re}^\ddagger$  2.7 kcal mol<sup>-1</sup> lower activation energy ( $\Delta E^\ddagger$ ) than that for  $(4-7)_{si}^\ddagger$ .

After having examined each elementary step in the catalytic cycle and shedding light on the origin of enantioselectivity in



Fig. 4 The overall Gibbs free energy profile (kcal mol<sup>-1</sup>) for the Rh-catalyzed asymmetric allylic alkylation of 2-phenylbutanal by allyl benzoate. The activation span ( $\delta E$ ) for different likely active catalysts is tabulated for comparison.







- 17 S. Grimme, J. Antony, S. Ehrlich and H. Krieg, *J. Chem. Phys.*, 2010, **132**, 154104–154119.
- 18 (a) P. C. Hariharan and J. A. Pople, *Theor. Chim. Acta*, 1973, **28**, 213–222; (b) V. A. Rassolov, J. A. Pople, M. A. Ratner and T. L. Windus, *J. Chem. Phys.*, 1998, **109**, 1223–1229.
- 19 (a) H. Stoll, P. Fuentealba, P. Schwerdtfeger, J. Flad, L. V. Szentpaly and H. Preuss, *J. Chem. Phys.*, 1984, **81**, 2732–2736; (b) M. Dolg, U. Wedig, H. Stoll and H. Preuss, *J. Chem. Phys.*, 1987, **86**, 866–872; (c) D. Andrae, U. Haussermann, M. Dolg, H. Stoll and H. Preuss, *Theor. Chim. Acta*, 1990, **77**, 123–141.
- 20 (a) C. Gonzalez and H. B. Schlegel, *J. Phys. Chem.*, 1990, **94**, 5523–5527; (b) C. Gonzalez and H. B. Schlegel, *J. Chem. Phys.*, 1989, **90**, 2154–2161; (c) K. Fukui, *Acc. Chem. Res.*, 1981, **14**, 363–368.
- 21 A. V. Marenich, C. J. Cramer and D. G. Truhlar, *J. Phys. Chem. B*, 2009, **113**, 6378–6396.
- 22 (a) I. Funes-Ardoiz and R. S. Paton, *GoodVibes*, v1.0.1, DOI: 10.5281/zenodo.56091; (b) S. Grimme, *Chem.-Eur. J.*, 2012, **18**, 9955–9964.
- 23 (a) R. F. W. Bader, *Chem. Rev.*, 1991, **91**, 893–928; (b) *AIM2000 Version 2.0*; Buro fur Innovative Software, SBK-Software, Bielefeld, Germany, 2002; (c) C. F. Matta and R. J. Boyd, *Quantum Theory of Atoms in Molecules: Recent Progress in Theory and Application*, Wiley-VCH, Weinheim, 2007.
- 24 (a) E. R. Johnson, S. Keinan, P. Mori-Sanchez, J. Contreras-García, A. J. Cohen and W. Yang, *J. Am. Chem. Soc.*, 2010, **132**, 6498–6506; (b) J. Contreras-García, E. R. Johnson, S. Keinan, R. Chaudret, J.-P. Piquemal, D. N. Beratan and W. Yang, *J. Chem. Theory Comput.*, 2011, **7**, 625–632.
- 25 (a) F. M. Bickelhaupt, *J. Comput. Chem.*, 1999, **20**, 114–128; (b) F. M. Bickelhaupt and K. N. Houk, *Angew. Chem., Int. Ed.*, 2017, **56**, 10070–10086; (c) F. Liu, Y. Liang and K. N. Houk, *Acc. Chem. Res.*, 2017, **50**, 539–543.
- 26 S. Kozuch and S. Shaik, *Acc. Chem. Res.*, 2011, **44**, 101–110.
- 27 The LiHMDS base exists as a trisolvated monomer in THF solvent, see:(a) B. L. Lucht and D. B. Collum, *Acc. Chem. Res.*, 1999, **32**, 1035–1042; (b) P. F. Godenschwager and D. B. Collum, *J. Am. Chem. Soc.*, 2007, **129**, 12023–12031.
- 28 (a) The cumulative strength of the NCIs in **A3** is found to be more efficient in making the *cis* disposition of the chiral ligands energetically more favorable over the corresponding *trans* arrangement in **A4**; (b) The details of the AIM analysis on **A3** and **A4** are provided in Fig. S1 and Table S1 in the ESI.†
- 29 The conversion of a phosphite ligand such as BINOL-P(OMe) to the corresponding phosphonate was suggested to occur in a Rh-catalyzed allylic alkylation of acyclic  $\alpha$ -alkoxy substituted ketones, see:P. A. Evans, E. A. Clizbe, M. J. Lawler and S. Oliver, *Chem. Sci.*, 2012, **3**, 1835–1838.
- 30 (a) The details of the Rh-Arbusov rearrangement with the other likely active catalyst from the **A** series are provided in Scheme S1 in the ESI;†For metal-catalyzed Arbusov rearrangement reactions, see:(b) T. B. Brill and S. J. Landon, *Chem. Rev.*, 1984, **84**, 577–585; (c) T. B. Brill and S. J. Landon, *Inorg. Chem.*, 1984, **23**, 4177–4181; (d) J. Ballester, J. Gatignol, G. Schmidt, C. Alayrac, A.-C. Gaumont and M. Taillefer, *ChemCatChem*, 2014, **6**, 1549–1552
- 31 An alternative mode of coordination through the phosphonate oxygen for the active catalyst **1** as well as in the Rh(III) intermediate (**4**) is respectively found to be 10.0 kcal mol<sup>-1</sup> and 4.5 kcal mol<sup>-1</sup> higher in energy as compared to the corresponding P-coordination.
- 32 For more details on lithium-based reagents in organic synthesis, see:(a) D. B. Collum, A. J. McNeil and A. Ramirez, *Angew. Chem., Int. Ed.*, 2007, **46**, 3002–3017Lithium reagent in a 1 : 1 mixture of THF and DMPU, see:(b) M. Ellwart, I. S. Makarov, F. Achraimer, H. Zipse and P. Knochel, *Angew. Chem., Int. Ed.*, 2016, **55**, 10502–10506; (c) X. Sun and D. B. Collum, *J. Am. Chem. Soc.*, 2000, **122**, 2452–2458For more details on enolate formation using LiHMDS, see:(d) P. Zhao, A. Condo, I. Keresztes and D. B. Collum, *J. Am. Chem. Soc.*, 2004, **126**, 3113–3118; (e) A. J. McNeil and D. B. Collum, *J. Am. Chem. Soc.*, 2005, **127**, 5655–5661; (f) For more details, see Scheme S2 in the ESI.†
- 33 (a) J. Clayden, F. E. Knowles and C. J. Menet, *Tetrahedron Lett.*, 2003, **44**, 3397–3400; (b) J. Clayden, F. E. Knowles and C. J. Menet, *Synlett*, 2003, 1701–1703; (c) J. Clayden, S. Parris, N. Cabedo and A. H. Payne, *Angew. Chem., Int. Ed.*, 2008, **47**, 5060–5062; (d) J. Clayden, W. Farnaby, D. M. Grainger, U. Hennecke, M. Mancinelli, D. J. Tetlow, I. H. Hillier and M. A. Vincent, *J. Am. Chem. Soc.*, 2009, **131**, 3410–3418; (e) A. M. Fournier, R. A. Brown, W. Farnaby, H. Miyatake-Ondozabal and J. Clayden, *Org. Lett.*, 2010, **12**, 2222–2225.
- 34 (a) All the likely combinations of oxidative addition were considered with **A1** as the potential active catalyst, where we found that the THF coordination to Li results in higher energy than the pathway without the inclusion of LiHMDS. The active participation of LiHMDS·1DMPU is found to lower the relative Gibbs free energies and hence LiHMDS·1DMPU has been considered explicitly for the computations for other potential active catalysts.For more details, see Table S2 in the ESI;†(b) Although the formation of (DMPU)<sub>3</sub>LiHMDS from (THF)<sub>3</sub>LiHMDS is found to be feasible, when the former binds to the catalyst–substrate complex (**3**), only one DMPU can remain coordinated. Attempts to locate transition state geometries with (DMPU)<sub>2</sub>LiHMDS resulted in immediate de-coordination of one of the DMPUs
- 35 The Gibbs free energy profile for the C–O bond oxidative addition with various likely active catalysts is provided in Fig. S2 in the ESI.†
- 36 (a) Different Rh-phosphonates with varying combinations of ligands could serve as the active catalyst. In the case of **B3**, the elementary step barrier for the C–O bond oxidative addition as well as the activation span is 0.9 kcal mol<sup>-1</sup> higher than that with **B1**; (b) In an interesting report, it was noted that the dissociation of one of the PPh<sub>3</sub> ligands resulted in a lower energy pathway, seeX. Deng, L.-Y. Shi, J. Lan, Y.-Q. Guan, X. Zhang, H. Lv, L. W. Chung and X. Zhang, *Nat. Commun.*, 2019, **10**, 949–959; (c) However, in the present system, the dissociative mechanism for the



